© 2017. Published by The Company of Biologists Ltd | Journal of Cell Science (2017) 130, 1845-1855 doi:10.1242/jcs.203877

TOOLS AND TECHNIQUES

# Microtubule organization within mitotic spindles revealed by serial block face scanning electron microscopy and image analysis

**Faye M. Nixon[1,2,*], Thomas R. Honnor[3,*], Nicholas I. Clarke[1], Georgina P. Starling[1], Alison J. Beckett[2], Adam M. Johansen[3], Julia A. Brettschneider[3], Ian A. Prior[2] and Stephen J. Royle[1,‡]**

## ABSTRACT

Serial block face scanning electron microscopy (SBF-SEM) is a powerful method to analyze cells in 3D. Here, working at the resolution limit of the method, we describe a correlative light–SBF-SEM workflow to resolve microtubules of the mitotic spindle in human cells. We present four examples of uses for this workflow that are not practical by light microscopy and/or transmission electron microscopy. First, distinguishing closely associated microtubules within K-fibers; second, resolving bridging fibers in the mitotic spindle; third, visualizing membranes in mitotic cells, relative to the spindle apparatus; and fourth, volumetric analysis of kinetochores. Our workflow also includes new computational tools for exploring the spatial arrangement of microtubules within the mitotic spindle. We use these tools to show that microtubule order in mitotic spindles is sensitive to the level of TACC3 on the spindle.

**KEY WORDS: 3D cell biology, Electron microscopy, Microtubules, Mitosis, Mitotic spindle, Statistics**

## INTRODUCTION

In readiness for cell division, eukaryotic cells build a mitotic spindle. This miniature machine, made of microtubules (MTs) and associated proteins, maneuvers the duplicated chromosomes and segregates them so that the two daughter cells each receive a complete copy of the genome. Understanding how this MT-based structure is organized and how it works is a major theme in cell biology (Petry, 2016).

In human cells, the mitotic spindle is a fusiform structure, which at metaphase is virtually spherical. MTs radiate from the two spindle poles, and belong to one of three classes: (1) astral MTs, which extend from the poles back towards the plasma membrane; (2) interpolar MTs, which run from one pole towards the other pole; and (3) kinetochore MTs, which are attached to the kinetochore on the chromosome (Mastronarde et al., 1993; McDonald et al., 1992; Helmke et al., 2013). Kinetochore MTs are bundled together to form kinetochore fibers (K-fibers) and, at metaphase, 20–40 MTs constitute a single K-fiber bundle (Booth et al., 2011, 2013; Sikirzhytski et al., 2014; McEwen et al., 1997). A network of crosslinking material, termed the 'mesh', is thought to hold kinetochore MTs together throughout their length (Hepler et al., 1970; Nixon et al., 2015). So far one protein complex containing TACC3, clathrin and ch-TOG (also known as CKAP5) has been identified as being a component of the mesh (Booth et al., 2011; Nixon et al., 2015).

The MTs of the mitotic spindle are densely packed and so resolving their organization in 3D is challenging. Advances in super-resolution imaging and expansion microscopy have improved the view of mitotic MTs that can be achieved by using light microscopy (Mikhaylova et al., 2015; Chozinski et al., 2016), yet the gold standard method is still electron microscopy (EM). Reconstructions of entire spindles in 3D using serial sectioning and transmission electron microscopy (TEM) have told us much about mitotic spindle structure (Mastronarde et al., 1993; McDonald et al., 1992; Redemann et al., 2016 preprint). However, these methods are extremely laborious, technically challenging, and prone to error. The advent of automated EM methods, such as serial block face scanning electron microscopy (SBF-SEM) has promised to speed up the analysis of complex cellular structures in 3D (Hughes et al., 2014). The spatial resolution of SBF-SEM is reported to be ∼10 nm, making it ideal for the study of MTs (25 nm diameter) in the mitotic spindle. Whether this resolution can be reached routinely for such analysis is unclear.

The first aim of the present study was to apply SBF-SEM to the problem of resolving MTs in the mitotic spindle. The resulting datasets are large and require robust statistical methods for analysis, and our second aim was, therefore, to provide computational tools to aid understanding of such datasets. The resulting workflow was then used to further understand how TACC3 levels influence MT organization in mitotic spindles.

## RESULTS

### Visualization and 3D reconstruction of mitotic spindle MTs

We began by finding the optimal conditions for imaging MTs in mitotic cells by SBF-SEM. These conditions, described in the Materials and Methods section, allowed us to image a volume containing almost the entire spindle and to visualize bundles of MTs in the spindle running from the pole to the chromosomes (Fig. 1). The resulting datasets could be segmented, rendered in 3D and analyzed computationally (Fig. 1A and Materials and Methods). This workflow resulted in the visualization of a 3D rendering of the mitotic spindle (Fig. 1B,C). Even under these optimized conditions, we were working at the resolution limit of the instrument and this hampered our ability to resolve every single MT in the mitotic spindle (see below). Where single MTs could be discerned, we were unable to resolve the ends of MTs (Fig. 1B). Such resolution is possible with TEM and tomography; however, those methods are incredibly labor intensive. While SBF-SEM has limitations, our simple and rapid workflow allows the accurate mapping of mitotic spindle architecture sampled beyond the resolution limit of light microscopy and also permits much higher throughput.

[1]Centre for Mechanochemical Cell Biology, Warwick Medical School, Coventry CV4 7AL, UK. [2]Institute for Translational Medicine, University of Liverpool L69 3BX, UK. [3]Department of Statistics, University of Warwick, Coventry CV4 7AL, UK.
*These authors contributed equally to this work

‡Author for correspondence (s.j.royle@warwick.ac.uk)

F.M.N., 0000-0002-7029-2649; I.A.P., 0000-0002-4055-5161; S.J.R., 0000-0001-8927-6967

**Received 14 March 2017; Accepted 31 March 2017**

Journal of Cell Science (2017) 130, 1845-1855 doi:10.1242/jcs.203877

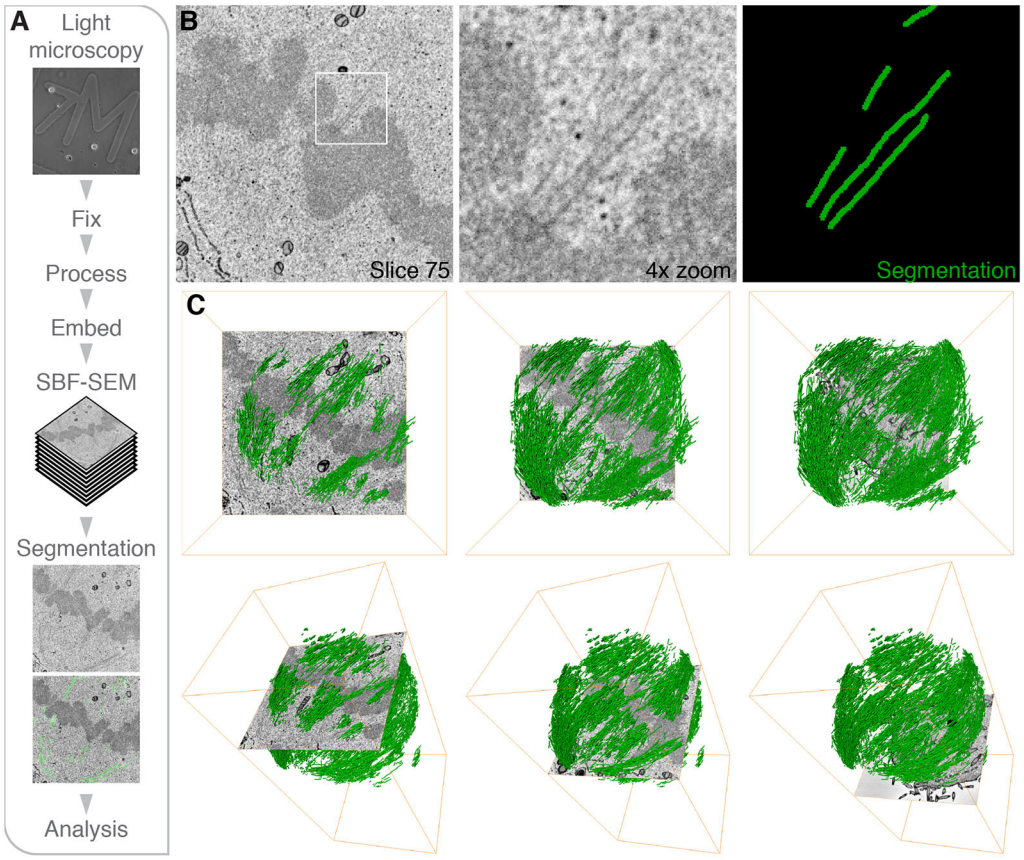


**Fig. 1. SBF-SEM of mitotic spindles.** (A) Practical workflow. A single mitotic cell on a gridded dish is first visualized by light microscopy (left) to assess its mitotic stage and transfection status. The cell is then fixed, processed and embedded for SBF-SEM. A series of SEM images are captured at 60 nm intervals through the block. Using Amira, the MTs are segmented along with any other cellular features. Analysis of segmentation data is carried out in Igor Pro or R. (B) A single SBF-SEM image is shown together with a 4× magnification and detail of segmented MTs (green). (C) 3D rendering of MTs in the mitotic spindle is shown with an orthoslice at three different depths (left to right), as *en face* (upper row) or tilted views (lower row).

### Limitations of MT mapping by SBF-SEM

Since the images were captured at the resolution limit of the instrument, a key question is whether or not we have single-MT resolution. To look at this, we focused on astral MTs, which are known, from serial section TEM experiments, to exist as single, isolated MTs (McDonald et al, 1992). Fig. 2A shows that clear density, attributable to individual astral MTs, can be identified in our images and easily segmented. This observation indicates that the method has single-MT resolution. We expected the detection of single MTs in regions of low MT density to be easier than discerning single MTs in the main body of the spindle. To examine MT detection in regions of higher density, we counted MTs that terminated at kinetochores and compared these numbers with previous observations undertaken with TEM (McEwen et al., 1998; 1997). On average, we resolved a median of six MTs terminating at the kinetochore [interquartile range (IQR)=5 (4–9); $n$=4 cells] (Fig. 2B–D; Movie 1). This varied somewhat between datasets, from four [IQR=3.5 (1.5–5)] to eight [IQR=4 (6–10)], but is fewer than the 20–23 MTs reported to be present at metaphase by serial section TEM (McEwen et al., 1998, 1997). Comparing the number of MTs at a given kinetochore with the number terminating at its sister, however, gave broadly comparable numbers (Fig. 2D). Assuming that the number of MTs at kinetochores does not vary substantially, this suggests that local differences in MT detection underlie the variability within a dataset. These data indicate that in higher density regions of the spindle, we do not have single-MT resolution. We conclude that detection of single MTs is possible, but that MT detection is not uniform throughout the volume. The sample of MTs that can be resolved is nonetheless substantial and sufficient for further analysis.

### Spatial statistics of MTs visualized by SBF-SEM

The large-scale high-resolution view of MTs resulting from our workflow was well suited for the development of geometric models to describe mitotic spindle organization. These methods and associated code are detailed in the Materials and Methods section, and an overview is presented here.

First, the volumetric density of MTs in the spindle could be determined. As an input, we take the segmented MTs from SBF-SEM data, and this is used to calculate the total volume of MTs. This value is then normalized to the volume of spindle, which is visible in the dataset (Fig. 3A). This normalization step is essential because at the magnification necessary to resolve MTs, the spindle volume is often incomplete. To test the sensitivity of this volume density calculation, we compared cells treated with cold (4°C) versus warm (37°C) media. When cells are treated with cold medium, any MTs which are not stably attached at both ends become depolymerized leaving only the K-fibers intact (Rieder, 1981). In HeLa cells, and in two different cell lines derived from glioblastoma patients, we measured a decrease in MT density to approximately one-third of the volume recorded in control cells in warm medium (Fig. 3B).

Second, the spatial organization of MTs in the spindle is analyzed. The aim is to determine the amount of order – or degree of alignment – for MTs in the mitotic spindle. To do this, an idealized spindle is generated computationally using the coordinates of the segmented MTs and simple geometric principles (Fig. 4 and Materials and Methods section). The measured angle between each MT segment and its idealized counterpart is calculated [$\theta^{(i)}$ in Fig. 4A]. For an ideal mitotic spindle, in which all microtubules are aligned, all angles will

Journal of Cell Science (2017) 130, 1845-1855 doi:10.1242/jcs.203877

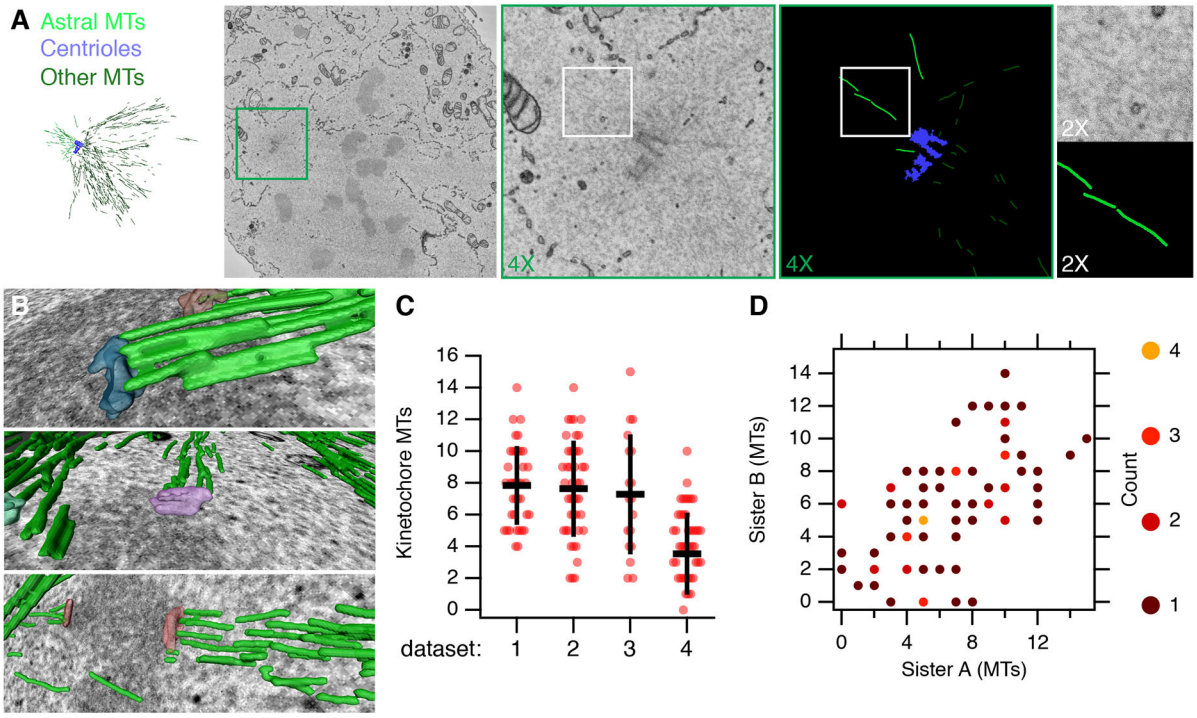


**Fig. 2. Single MTs can be resolved in subsections of SBF-SEM image stacks.** (A) Overview of a spindle pole from a HeLa cell at late prometaphase. Astral MTs are rendered in light green, other MTs in darker green and centrioles are rendered in blue. A 3D rendering of slices 86–104 is shown on the left. Slice 92 is shown in the second panel followed by the indicated zooms of the SEM image and segmentation (4× equals a window size of 4.6 µm, 2× equals a window size of 1.15 µm). (B) 3D rendering of example kinetochores and their associated K-fibers (green). (C) Quantification of segmented MTs that terminate at kinetochores. Four datasets are shown from control cells, indicating the variability in detection. Spots are individual kinetochores, bars indicate mean±s.d. (D) A plot of kinetochore microtubules counted at a given kinetochore versus the number at the sister kinetochore. Overlapping points are highlighted by color as indicated.

equal 0°. For real mitotic spindles, the angles deviate considerably from the ideal. Therefore, the magnitude of the angle deviations from the idealized spindle indicate a departure from perfect alignment. For example, the microtubules in the control GFP-expressing cell shown throughout this paper have a median angle of 11.2° [IQR=14.8° (5.2–20.0°)] (Fig. 5A). Previously, we found that overexpression of TACC3 caused changes in the degree of alignment of MTs (Nixon et al., 2015). These conclusions were based on tomography of a single thin section cut orthogonally to the K-fiber axis. Our new statistical method meant that this comparison could now be done on a near-global and whole-spindle scale. To look deeper into this phenomenon, we wanted to increase or decrease the TACC3 levels on the spindle and examine changes in the amount of MT order. Therefore, in addition to GFP-expressing control cells, we processed cells conditionally overexpressing GFP–TACC3 and also cells where the endogenous TACC3 was depleted by use of a shRNA but also expressed a mutated form (S558A) of GFP–TACC3 that was refractory to the shRNA. This mutant cannot bind clathrin and therefore cannot localize to the mitotic spindle (Hood et al., 2013). These three genotypes were examined in both warm and cold conditions (Fig. 5C; Fig. S1). Deviations from the ideal were compared using $\Pi(\Theta_1, \Theta_2)$ for all combinations of data (see Materials and Methods section for further details). This comparison of angle deviations from these datasets showed that mitotic spindles in cells with more TACC3 had less order than controls under warm conditions (Fig. 5A,C). Similar deviations were seen in the cells expressing TACC3(S558A) in place of endogenous TACC3. This analysis extends, and is in agreement with, our previous conclusion that MT order in mitotic spindles is influenced by TACC3 levels on the mitotic spindle (Nixon et al., 2015). The comparison between warm- and cold-treated samples revealed that MTs in cells expressing TACC3(S558A) in place of endogenous TACC3 were more disorganized after cold treatment. Interestingly, the cold-treated cells overexpressing TACC3 did not show the same phenotype. The amount of order for MTs in this condition was similar to cold-treated GFP-expressing cells, which may suggest that elevated TACC3 levels protect MTs against cold-induced changes in spatial organization.

### Volumetric analysis of kinetochores

SBF-SEM datasets also allowed the segmentation of kinetochores, and therefore the calculation of their volume (Fig. 6). The average volume of a kinetochore was $8.17\times10^6\pm0.3\times10^6$ nm$^3$ (mean±s.e.m.). The surface area of the outer face of the kinetochore, as measured by serial section TEM is 0.16±0.05 µm$^2$ (McEwen et al., 1998), which would mean a thickness of 50 nm. This is very similar to the thickness in our segmented images, indicating agreement and accurate quantification. Since the pairing of kinetochores can be easily determined in the dataset, we tested the idea that sister kinetochores have similar volumes and that kinetochore volumes vary across the dataset. A plot of sister kinetochore volumes is shown in Fig. 6C. One-way ANOVA indicated that there were significant differences between pairs of kinetochores [$F(33,34)=1.918$, mean squared error (MSE)=$4.6\times10^{-12}$, $P=0.032$]. Randomization of the data and retesting by one-way ANOVA gave further confidence to this result (Fig. 6D). These findings suggest that large kinetochores are paired with large kinetochores and small kinetochores with small kinetochores.

Journal of Cell Science (2017) 130, 1845-1855 doi:10.1242/jcs.203877

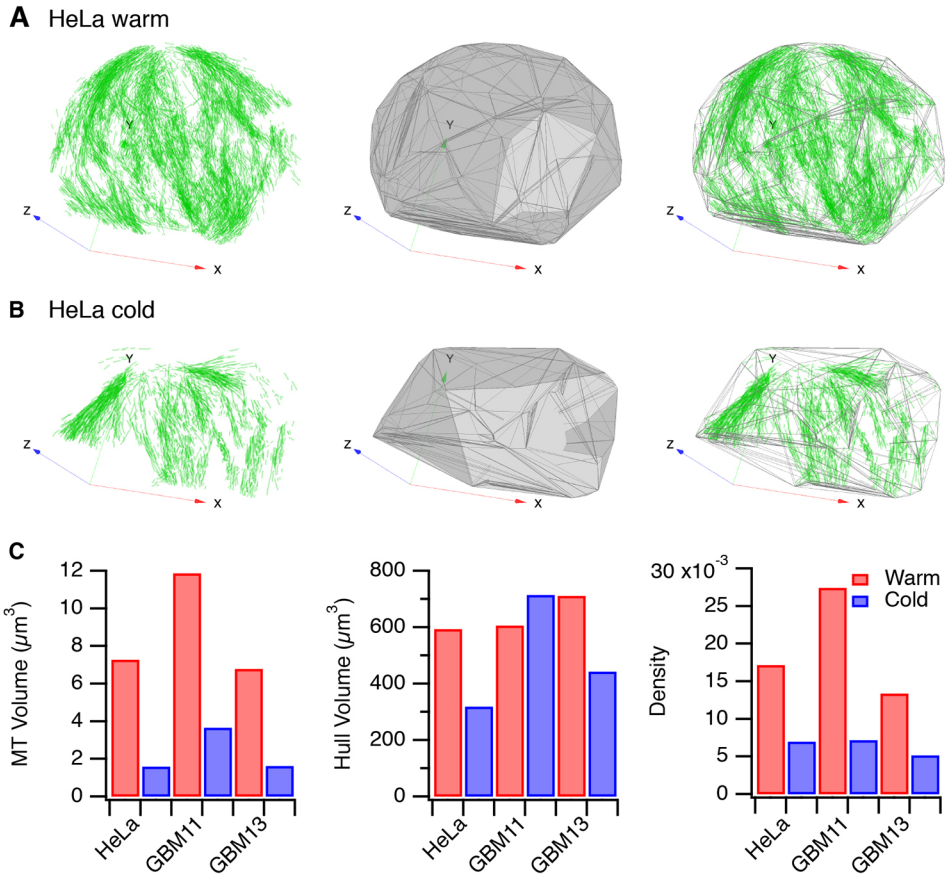


**Fig. 3. Volume calculations for mitotic spindles.** (A) Map of MTs in a HeLa cell at metaphase. A 3D convex hull is drawn around all points in the map and used for volume calculation and normalization of MTs into a density. The same cell is shown in Fig. 1. (B) Map of MTs in a cold-treated HeLa cell at metaphase. (C) Plots of MT volume, hull volume and density (MT volume/hull volume) for three different cell types. A comparison of warm (red) versus cold (blue) is shown. *n*=1 cell per condition.

### Two further observations from SBF-SEM of mitotic cells – spindle encapsulation and bridging fibers

In addition to the mitotic spindle and associated chromosomes, the membranes of mitotic cells could also be rendered in three dimensions. This allowed us to explore the relationship between intracellular membranes and the mitotic spindle. We found that the mitotic spindle was situated within an 'exclusion zone' that was largely free of membranes and organelles (Fig. 7; Fig. S2, Movie 2). Outside of this zone, the endoplasmic reticulum (ER) was densely packed and mitochondria were distributed within the folds of ER. These observations agree with previous work that described the organization of ER membranes in mitotic cells (Puhka et al., 2007, 2012) and with more recent work that proposed that, although mitosis in human cells is open, the spindle is encapsulated by membrane (Schweizer et al., 2015). The purpose of this encapsulation is to exclude organelles and concentrate the proteins necessary to build a mitotic spindle rapidly (Schweizer et al., 2015).

While studying the organization of MTs in the mitotic spindle, we also had the opportunity to look for the presence of 'bridging fibers'. These small bundles of MTs have been proposed to span from one K-fiber emanating from one pole, across the sister kinetochores and to reach the K-fiber that emanates from the opposing pole (Kajtez et al., 2016; Tolić and Pavin, 2016). Close inspection of our segmented datasets showed the presence of structures which may correspond to bridging fibers. Examples are shown in Movie 3 and a single example is shown in Fig. 8. We could not find evidence for bridging fibers associated with every K-fiber pair, although this is probably because our coverage is incomplete rather than an indication that there is not a one-to-one association of bridging fibers with each K-fiber pair.

## DISCUSSION

SBF-SEM is commonly used to examine cellular and multicellular structures on the scale of tens to hundreds of micrometers. Whether or not this mode of imaging could discern small subcellular structures such as MTs (25 nm diameter) in complex networks such as the mammalian mitotic spindle was untested. Our results indicate that it is possible to visualize a large sample of MTs in the mitotic spindle of a human cell. The resulting datasets were complex and required robust analytical tools, which were developed and presented as part of this paper. We applied our workflow to test the influence of the levels of TACC3 at the mitotic spindle on the organization of MTs on a whole-spindle scale.

The influence of TACC3 on mitotic spindle structure has previously been examined by using two extreme methods. In the first, individual high magnification views of subsections of the spindle were obtained by means of electron tomography (Nixon et al., 2015). Second, low spatial resolution views of whole spindles were captured by light microscopy (Hood et al., 2013; Gergely et al., 2000). What was missing was a technique that combines the advantages of both methods to visualize MT order on the scale of the whole-mitotic spindle. Super-resolution methods cannot currently fulfill this gap, and the present study shows that SBF-SEM can, and that it does so at an appropriate scale to answer questions about MT organization. Moreover, the automation of the image capture and data processing means that it is practical to analyze spindles in this way. While the resolution of this method is lower than TEM and electron tomography, its power lies in the higher throughput and lower requirement for technical expertise. SBF-SEM is not suitable for answering questions that absolutely

Journal of Cell Science (2017) 130, 1845-1855 doi:10.1242/jcs.203877

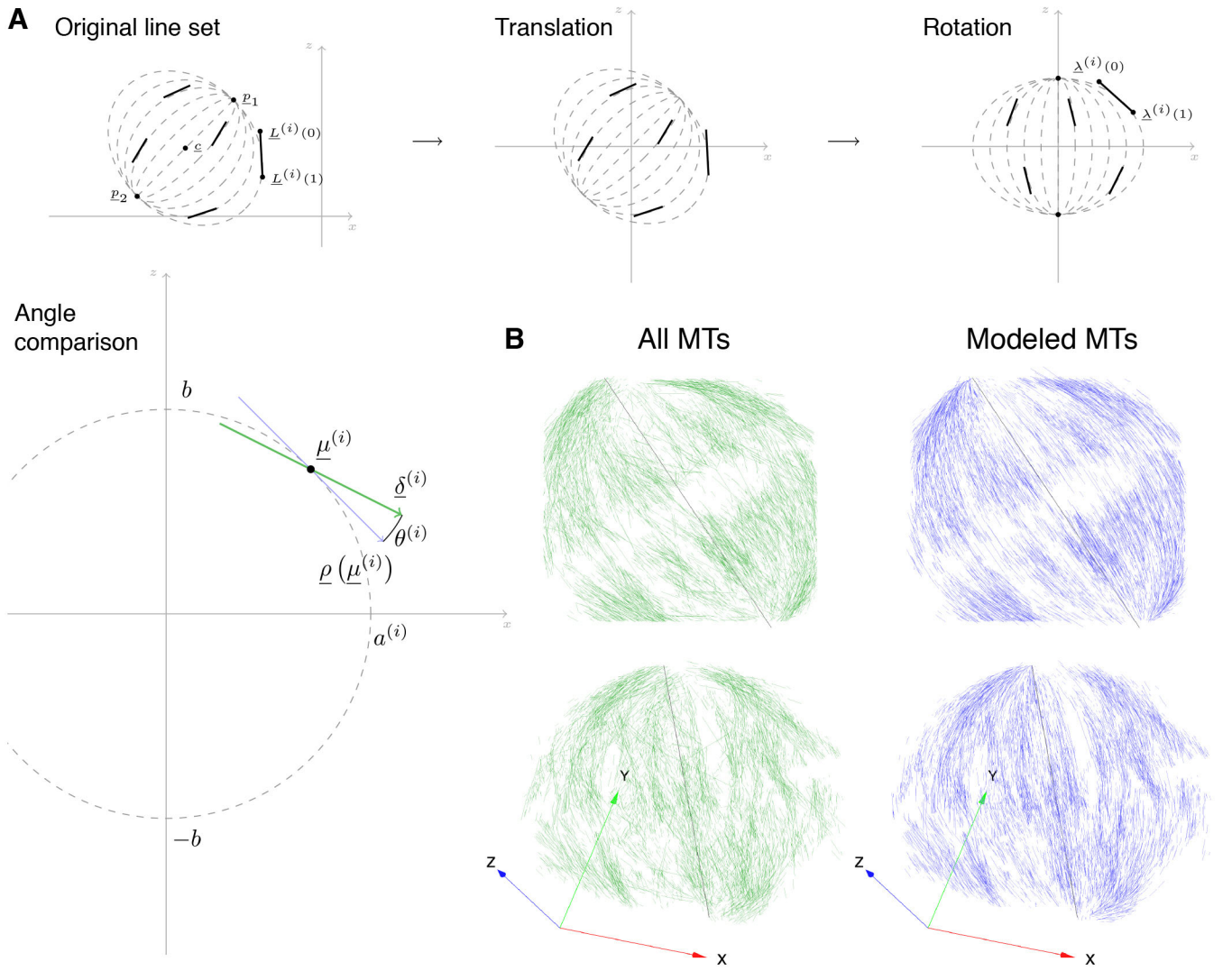


**Fig. 4. Using a simple geometric model to obtain idealized mitotic spindles from measurement data.** (A) Schematic diagrams to illustrate how the idealized mitotic spindles were generated. The real data set is translated and rotated so that the spindle is stood up, with the spindle poles aligned on the *z*-axis at *x*=*y*=0. Ellipsoids that pass through the spindle poles are generated for the midpoint of each MT, and the tangent is used to generate the idealized MT counterpart. The angle between the real and ideal line is recorded for each MT. (B) An example of an idealized model spindle (blue, right) was created from the MT positions in a real data set (green, left). The spindle is shown in *en face* (XY view, upper) and tilted (lower) views. Deviations of the real data from the model spindle were measured by taking the angle of real MTs versus their idealized counterpart. The cell from which this data derives is shown in Fig. 1.

require single MT resolution and, particularly, the resolution of MT ends (McIntosh et al., 2013); however, it can compete with TEM and electron tomography. We showed that 35 pairs of kinetochores could be easily segmented from a single SBF-SEM dataset, a number sufficient to test whether or not sister kinetochores were of a comparable size. Capturing a similar dataset by serial section TEM would be extremely challenging and laborious, with no clear resolution advantage in this case.

Our analytical workflow allowed us to assess MT density and MT order. While it is possible to approximate the volume of MTs in cells using light microscopy, the higher resolution of SBF-SEM provides more precise quantification of the MT volume in a mitotic cell. Determining the order of MTs in a dense array is not currently possible by light microscopy, even in super-resolution modes, and the advantage of SBF-SEM, here is therefore clear. The simple description that we developed was based on comparison with an idealized spindle. We found that ellipsoids were a good model for angular comparison, out-performing other geometric shapes and comparison regimes based on near-neighbors or on the spindle axis (see Materials and Methods).

Our data indicate that too much TACC3 (or too little) affects MT order in mitotic spindles. Previous work has shown that mitotic progression is slowed in cells overexpressing TACC3 or in cells depleted of TACC3 through expression of siRNA (Nixon et al., 2015; Gergely et al., 2003; Lin et al., 2010). The current picture is that the major function of TACC3 in mitotic spindles at metaphase is as part of a TACC3–ch-TOG–clathrin complex that is assembled upon Aurora A-mediated phosphorylation, rather than as a MT plus-tip protein. The TACC3–ch-TOG–clathrin complex is an important component of the 'mesh' that is thought to maintain the integrity of the K-fiber MTs. The present data indicate that the sensitivity of mitosis to TACC3 levels is because of changes in the composition of the mesh that, in turn, alters K-fiber structure and organization; it strongly suggests that these changes prevent the chromosome

Journal of Cell Science (2017) 130, 1845-1855 doi:10.1242/jcs.203877

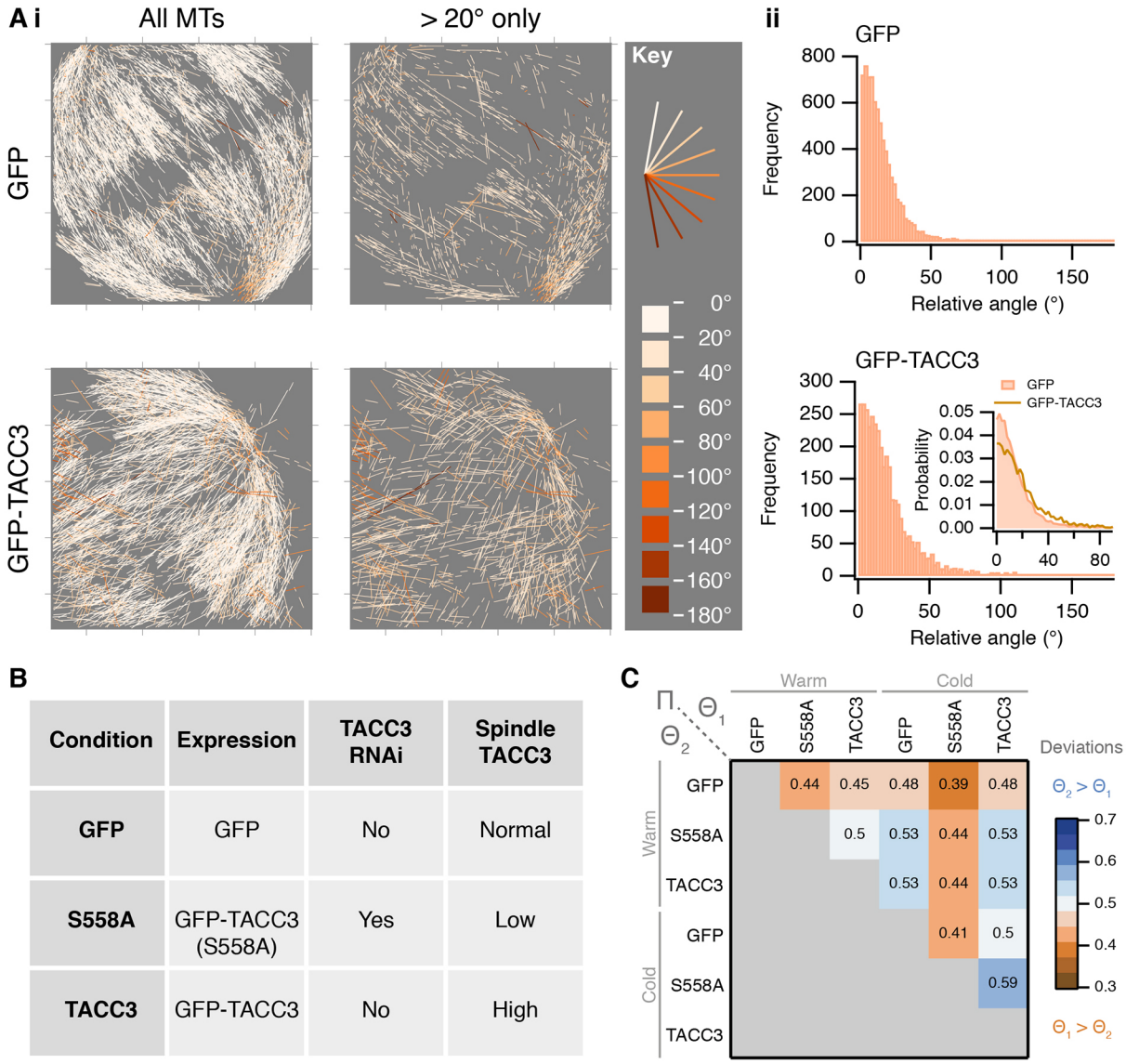


B

| Condition | Expression | TACC3 RNAi | Spindle TACC3 |
|---|---|---|---|
| **GFP** | GFP | No | Normal |
| **S558A** | GFP-TACC3 (S558A) | Yes | Low |
| **TACC3** | GFP-TACC3 | No | High |




**Fig. 5. A statistic for microtubule order in mitotic spindles.** (A) Two examples of angle analysis. (i) MTs from a control cell and a cell overexpressing GFP–TACC3 are shown colored according to their deviation from the respective model spindle. In the right panel, MTs with deviations of less than 20° have been removed for clarity. The plots show a *z*-projection of the entire volume. (ii) Histogram of angle deviations for the spindles. Inset: comparison of the two histograms shown as a normalized probability density function. (B) Summary of cellular conditions analyzed under warm and cold conditions. (C) Heat map to show $\Pi(\Theta_1, \Theta_2)$ for several conditions as indicated. $\Pi$ is a comparison of angles from two data sets: values greater than 0.5 indicate that $\Theta_2$ MTs deviate more from the ideal data than those in $\Theta_1$ (see Materials and Methods, Model discrepancy and comparison for further details). *n*=5031–23240 segments from 1–4 cells. All datasets in this figure are shown in Fig. S1.

movements required for high-fidelity mitosis. However, we cannot exclude the possibility that other functions of TACC3 contribute to MT order or to mitotic progression.

These 3D views of mitotic cells also allowed us to visualize the spindle exclusion zone and putative 'bridging fibers' of the mitotic spindle. Clearly distinguishing bona fide bridging fibers from other microtubules is challenging, even at this resolution. Some examples presented here clearly look like bridging fibers that run in parallel to the respective sister K-fibers (Kajtez et al., 2016; Tolić and Pavin, 2016). Others highlighted in Movie 3 were less clear. If these structures are not bridging fibers, they could be interpolar MTs or K-fiber MTs, which are laterally or merotelically attached to kinetochores (Cimini et al., 2001). A formal test to determine whether these MT bundles are associated with the sister K-fibers will require TEM analysis.

Analysis of MT order by SBF-SEM requires operating at the resolution limit of the instrument. We optimized the staining of the sample, section depth, the magnification and accelerating voltage/beam energy to be able to visualize MTs. This protocol allowed us to sample a large fraction of MTs in the spindle, but fell short of a complete view of the mitotic spindle for three reasons. First, the spindle volume was incomplete since the magnification required to see MTs resulted in an *xy* area of 9.2×9.2 µm, although this limitation can be circumvented by stitching fields-of-view for each slice. Second, we could only resolve single MTs in parts of the dataset; however, in denser regions, we were unable to resolve all MTs. For example, we found fewer than the expected numbers of MTs terminating at each kinetochore. Third, the section depth of 60 nm resulted in missing MT information. The step size matched the beam penetration depth, because heavily stained objects such as

Journal of Cell Science (2017) 130, 1845-1855 doi:10.1242/jcs.203877

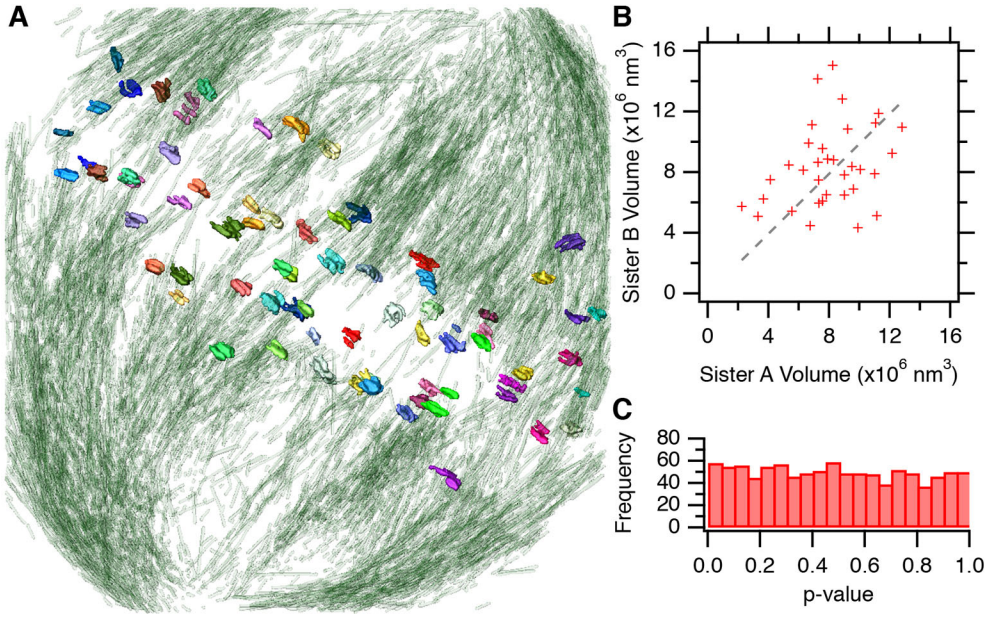


**Fig. 6. Volumetric analysis of kinetochores.** (A) Overview of kinetochores segmented in a single cell (shown in Fig. 1). Segmented MTs are rendered in dark translucent green; kinetochores are multicolored 3D rendered volumes. (B) Plot of volumes calculated from segmentation of kinetochores in a mitotic cell. 72 kinetochore volumes were calculated and clear sister pairs were discernible for 70. Classification of sister kinetochores as A or B is arbitrary. The dotted line shows a fit $y=a+bx$, if $a=0$, b=0.99±0.06 (±s.d., coefficient of determination $r^2=0.89$). (C) Histogram of *P*-values from one-way ANOVA tests on 1000 randomizations of the same kinetochore volume dataset. $0<P<0.05$ is not more frequent than any other interval.

membranes could be accurately followed with no under- or over-sampling. However, thin objects such as MTs that are weakly stained appear discontinuous, presumably because they are only visible at the upper surface of the block. Note that the spindle exclusion zone actually improves MT visualization because the organelle-free zone does not interfere with MT detection and segmentation. Thinner sectioning, possibly using focused ion beam SEM, would improve visualization further. For these reasons, one

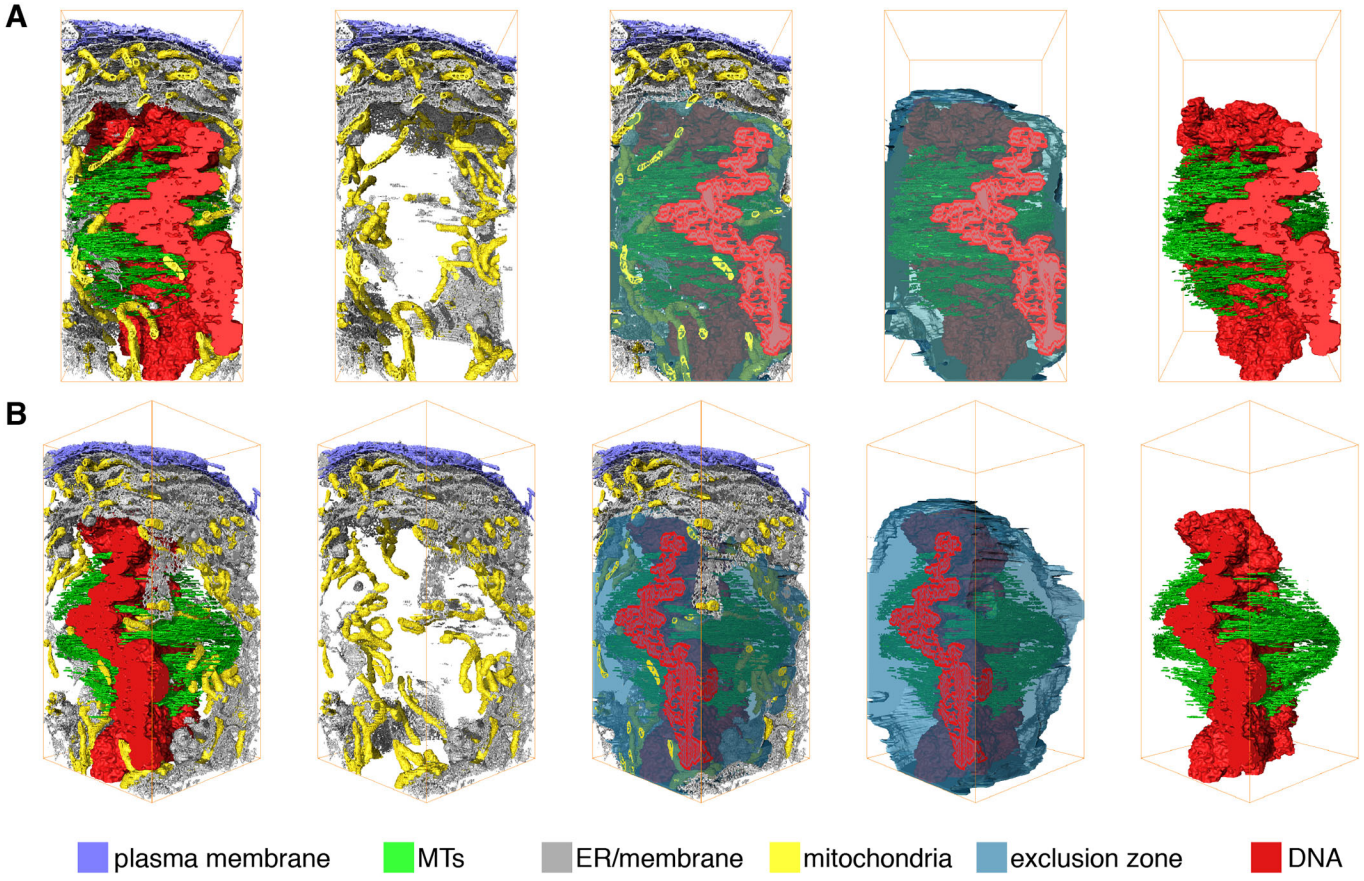


**Fig. 7. The spindle exists in an 'exclusion zone'.** 3D rendered model of a mitotic cell at metaphase to show the organization of membranes relative to the mitotic spindle. Subcellular structures that are rendered in 3D are: chromosomes (red), mitotic spindle microtubules (green), mitochondria (yellow), plasma membrane (purple), and endoplasmic reticulum and other membranes (gray). An 'exclusion zone' is modeled as a translucent blue bubble. The view in A is rotated 45° about the *z*-axis to give the view in B. A larger version of this figure with more rotations is shown in Fig. S2.

Journal of Cell Science (2017) 130, 1845-1855 doi:10.1242/jcs.203877

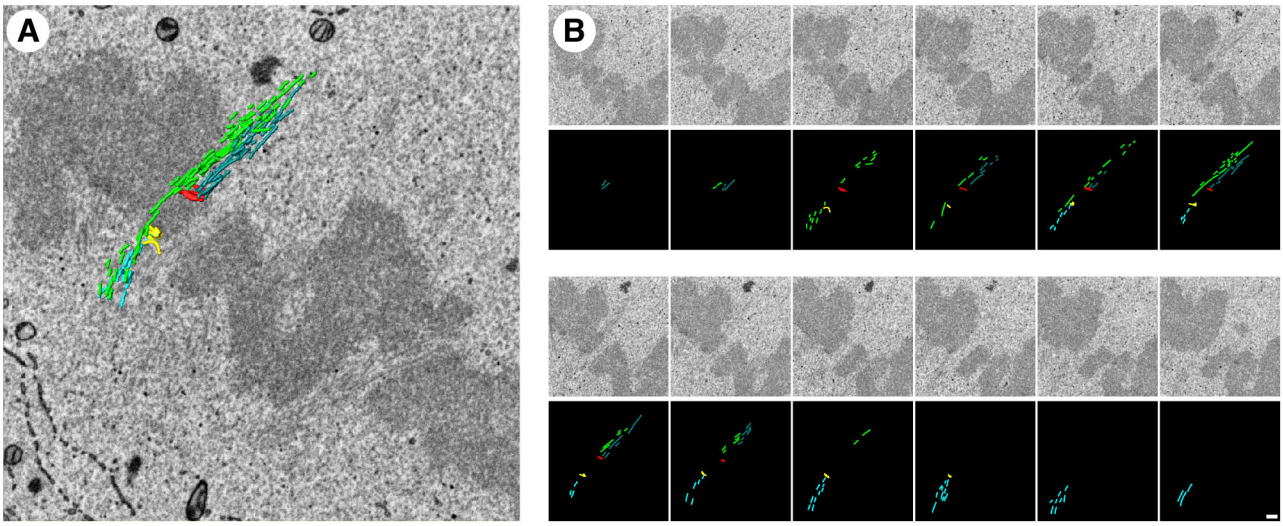


**Fig. 8. Example of a putative bridging fiber.** (A) A single SBF-SEM image is shown of the area of interest, with a 3D model of microtubules and kinetochores overlaid. Opposing sister kinetochores (red and yellow) are connected to K-fibers (dark blue and light blue, respectively). (B) Sequential SEM images (above) with segmentation (below) that make up the image shown in A. Each image is separated by 60 nm in the *z* direction. Note that, in this example, the bridging fiber runs on the exterior of the spindle not the interior as predicted (Kajtez et al., 2016). A movie showing putative bridging fibers is shown in Movie 3.

caveat associated with the method presented here is that the analysis is performed on only a subset of the MTs in the mitotic spindle. We believe that this subset is a good representation of the mitotic spindle: it was sufficient to show differences in MT density and changes in MT order in the mitotic spindle. Future directions for better detection of MTs in mitotic cells include improved SEM detector technology and high-pressure freezing as a fixation method. It remains to be seen whether any of these innovations would allow full reconstruction of the mitotic spindle. While improvements in detection may allow greater coverage, the protocol presented here is sufficient for large-scale analysis of MT order in human cells; and in higher throughput than traditional EM methods.

## MATERIALS AND METHODS

### Cell biology

HeLa cells that overexpress TACC3 upon doxycycline induction were as described previously (Nixon et al., 2015). Cells were maintained in Dulbecco's modified Eagle's medium (DMEM) plus 10% fetal bovine serum (FBS) and 1% penicillin-streptomycin in a humidified incubator at 37°C and 5% $CO_2$. The cell culture medium was further supplemented with G418 (300 µg ml$^{-1}$) for the parental HeLa TetOn cells, and with G418 and Hygromycin B (200 µg ml$^{-1}$) for the HeLa TetOn cells stably transfected with the TACC3 plasmid. Glioblastoma cell lines were cultured in neurobasal medium, supplemented with B27, N2, human fibroblast growth factor (40 ng ml$^{-1}$) and human epidermal growth factor (40 ng ml$^{-1}$).

For experiments to express GFP–TACC3(S558A), we used a plasmid (pBrain-GFP-TACC3(S558A)KDP-shTACC3) which knocks down the expression of endogenous TACC3 and simultaneously expresses GFP–TACC3(S558A), which is refractory to the shRNA (Gutiérrez-Caballero et al., 2015). Cells were transfected using GeneJuice, according to manufacturer's instructions.

Three HeLa conditions were studied: first, parental HeLa TetOn cells transiently transfected with pEGFP-C1 only as a control; second, the inducible GFP–TACC3-expressing HeLa TetOn stable cell line; third, parental HeLa TetOn cells transiently transfected with the pBrain-GFP-TACC3(S558A)KDP-shTACC3 construct. Cells were synchronized by thymidine-Ro3306 treatment (Nixon et al., 2015) and grown on gridded dishes (MatTek) to allow correlation between light and electron microscopy images. Synchronization using thymidine-Ro3306 is preferred to nocodazole or similar drugs, which perturb microtubules. For cold treatment of mitotic cells, cells were imaged to ensure the cells were at metaphase, and the growth medium was removed and replaced with ice-cold growth medium and incubated on ice for 10 min. Medium was then replaced with cold fixative.

### Electron microscopy

Fluorescence imaging was performed using a Nikon Eclipse Ti-U microscope with standard filter sets for visualization of GFP. Light and epifluorescence micrographs were acquired by using a Photometrics Myo camera, with 20× air and 60×oil objectives, and NIS Elements acquisition software. Cells were imaged in a 37°C temperature-controlled chamber (OKOlab). Chemical fixation, processing and sectioning for TEM, was performed as described previously (Booth et al., 2013). To prepare samples for SBF-SEM, the cells were also processed in a correlative manner to ensure only metaphase cells expressing the protein of interest were chosen. Processing was as described in Booth et al., 2013 with the following extra steps to better visualize ultrastructural components of the cell by SEM. Formaldehyde (0.5%) and glutaraldehyde (3%) fixative solution was prepared in phosphate buffer (0.1 mol l$^{-1}$), with 0.1% tannic acid and 3% sucrose. Two osmication steps were performed. First, a 1 h reduced osmium step, where 2% $OsO_4$ was prepared in 1.5% potassium ferrocyanide solution, in phosphate buffer. After five 3-min dd$H_2O$ washes, 0.1% thiocarbohydrazide (TCH) was added for 30 min at 60°C as a mordant. After another five 3-min dd$H_2O$ washes, $OsO_4$ (2% in dd$H_2O$) was applied for 30 min. The cells were again washed in water as before, then stained overnight using 1% uranyl acetate in dd$H_2O$ at 4°C. The following day, water washes were repeated before incubating with lead aspartate at 60°C for 30 min. The cells were then dehydrated using graded ethanol. Cells were infiltrated using Epon 812 Hard premixed resin kit (TAAB). Once fully polymerized (48 h at 60°C), the dish and coverslip were removed and the cell located. This area was then excised using a junior hacksaw and razor blades to leave an ∼2 mm$^3$ piece of resin containing the cell. This cube of resin was mounted using Silver Dag onto a cryo pin which fits into the chuck of the 3View platform (Agar Scientific). The area around the cell was fine-trimmed using fresh glass knives, this produced an ∼100 µm$^2$ block face. Once trimmed, the block was coated with a silver paint using an eyelash, before a 15 nm gold–palladium coating was evaporated onto the block surface, again to reduce surface charging (Quorum Technologies, East Sussex, UK). The cell was imaged using the Gatan 3View System and Digital Micrograph software (Gatan, Abingdon,UK) and FEI Quanta 250 (FEI, Eindhoven, Netherlands). When aligned, the 3View machine was

Journal of Cell Science (2017) 130, 1845-1855 doi:10.1242/jcs.203877

allowed to cut-and-image the block surface, with 100 nm z-slices, initially optimizing the contrast and magnification for that particular block, before leaving the platform to run until the cell was fully sectioned and imaged. A 768×768 pixel image, 60 nm sections, 60 µs pixel dwell time, 2.1 keV and 21,000× magnification (12 nm pixel size, 9.216×9.216 µs) was optimal for imaging the spindle zone. These conditions needed to be fine-tuned for the individual sample, and were a compromise between reduced levels of sample charging, magnification and resolution.

### Image analysis

All 3D segmentation and surface rendering was performed with Amira software (Visualization Sciences Group, FEI). The voxel size in nm was entered upon loading of the file into Amira. MTs in SBF-SEM volume stacks were segmented manually in Amira by tracing all the MTs visible in each slice throughout the entire volume, this segmentation was rendered to generate a 3D surface. In addition, where membranes, chromosomes, kinetochores and centrioles were visible, these were segmented in a semi-automated manner, using pixel density to segment objects in 3D. The signal-to-noise ratio of segmented MTs was 3.5±0.4 (mean±s.e.m., $n$=1373 images), i.e. lower than electron tomographic data, which hampered automatic tracing (Weber et al., 2012). The segmentation files (*.am files) were processed in ImageJ/FIJI to create binary images that could be fed into Igor Pro 7.0. Code for analysis was custom-written in Igor Pro 7.0 and can be found at https://github.com/quantixed/VolumeFinder. For volume analysis, the image stacks are interpreted and pixels above threshold are counted for each slice of the stack. A 3D convex hull is drawn around all points to measure the volume for normalization. For ellipsoid comparison, described in detail below, the images are skeletonized in ImageJ/FIJI. This process converts each MT segment into a 1 pixel thick object. Each object is read by Igor and converted to a unique 2D vector by fitting a line $y=a+bx$ to the $xy$ coordinates of the object. All objects lie in the plane of the section/image and so a 2D vector is sufficient. The resulting straight lines are used for mathematical modeling. The modeling and comparison was performed in Igor Pro7.0 for code, see https://github.com/quantixed/VolumeFinder. To ensure reproducibility, and for error-checking, the modeling and analysis was independently rewritten in R using the $xyz$ coordinates of straight lines as an input. This code is also available at https://github.com/quantixed/VolumeFinder, where a detailed walkthrough document is also provided.

### Mathematical modeling

A more detailed description follows; in summary, straight lines (representing MT segments from the SBF-SEM dataset) were compared to computer-generated counterparts that were placed in the ideal location. All straight lines were translated and rotated such that the spindle was vertical with the poles aligned on the $z$-axis and the center of the spindle at the origin. The midpoint of each straight line was used to make an ellipsoid that passes through this point and through both spindle poles. The tangent of a section through this ellipsoid at the midpoint was used for comparison with the original straight line. This was done after putting the straight lines and the idealized counterparts back in their original location, and projecting both segments onto a single $xy$-plane. We developed this analysis method because the spindle is a fusiform structure, and therefore comparison of each MT segment to the spindle axis gave a broad range of deviations that made comparisons between conditions impossible (Fig. S3). Angle comparisons between each MT segment and its neighboring segments were not representative since MT density was not uniform throughout the volume (Fig. S3). The calculations for ellipse comparison rely on simple geometric principles and make use of the specified locations of the two spindle poles. This is possible because the force balance in the metaphase spindle ensures a symmetrical arrangement: the chromosomes are situated approximately at the equator, and the spindle poles are equidistant from the metaphase plate. A more simplified model, with a straight-line or diamond-shaped spindle, was less realistic than ellipses (Fig. S3). More complex curves are likely to yield a better fit, and are possibly justified in light of data showing that MTs do not necessarily extend from the spindle pole to kinetochore (Sikirzhytski et al., 2014; Elting et al., 2014); however, the inclusion of more parameters is not desirable.

### Observed lines

We observe a collection of straight lines, $i\in\{1, 2,n\}$, denoted $\underline{L}^{(i)} := (L_x^{(i)}, L_y^{(i)}, L_z^{(i)})$. Each line may be summarized by its two endpoints; $\underline{L}^{(i)}(0)$ and $\underline{L}^{(i)}(1)$; switching the labels of endpoints $\underline{L}^{(i)}(0)$ and $\underline{L}^{(i)}(1)$ results in the same line object. The section Translation and rotation justifies a particular choice of $\underline{L}^{(i)}(0)$ and $\underline{L}^{(i)}(1)$.

Line locations and orientations are determined from a stack of images collected at increasing depth through the cell with each line segment being extracted from a single image within this stack as described under Image analysis. The co-ordinate axes are aligned such that the image planes are perpendicular to the $z$-direction.

### Elliptical model

We wish to compare observed lines to paths lying on the surface of an ellipsoid model. In fact, we restrict ourselves to spheroids (i.e. ellipsoids with rotational symmetry about the $z$-axis) because we do not expect there to be any promotion/restriction to MT growth in either the $x$- or $y$-directions. The surface of such a spheroid centered at the origin contains all vectors of the form $\underline{v} = (v_x, v_y, v_z)$ such that:

$$\frac{v_x^2 + v_y^2}{a^2} + \frac{v_z^2}{b^2} = 1. \quad (1)$$

Proposed paths are geodesic curves on the surface of an ellipsoid described by (Eqn 1) which pass through the points (0,0, $b$) and (0,0,–$b$). Fixing the value of $b$ ensures that each path passes through a common pair of points, which model the mitotic spindle poles. This modeling is justified biologically since the force balance of the metaphase spindle ensures that the poles are approximately equidistant from the chromosomes at the equator. The remaining principal semi-axis length, $a$, is allowed to vary between paths, with $a^{(i)}$ used to denote the value associated with the line indexed by $i$, ensuring that every point in the plane $z$=0 is associated with the unique path that passes through it, representing the unique proposed trajectory of the MT that attaches to a theoretical chromosome at that location.

The formula given in (Eqn 1) describes a spheroid centered at the origin and aligned with the co-ordinate axes. However, while we expect our observed lines to be related these trajectories, we do not expect them to be centered and aligned. It is possible to transform the model to match the location and alignment of the observed data. We choose instead to transform the observed data for later ease of interpretation and presentation.

### Translation and rotation

Each observed line-segment is first translated so that the origin of the spheroid whose tangent-plane contains it is centered at the origin and then rotated so that this spheroid is aligned with the coordinate axes. This process begins by identification of two fixed points, $\underline{p}^{(1)}$ and $\underline{p}^{(2)}$, which after translation and rotation will become (0,0, $b$) and (0,0, –$b$) respectively. The location of these fixed points can be determined directly from the images themselves, in the case where the centrosomes are visible. Where centrosomes are not directly visible, they were inferred using the orientation of observed lines and the assumption that $\underline{p}^{(1)}$ and $\underline{p}^{(2)}$ are the spindle poles from which all MTs should originate.

The translation shifts the center of the straight line joining $\underline{p}^{(1)}$ and $\underline{p}^{(2)}$ to the origin by subtracting the center $\underline{c} = (\underline{p}^{(1)} + \underline{p}^{(2)})/2$ of the spheroid from each observation. Rotation about the line through the origin, which is perpendicular to both the $z$-axis and the line-segment connecting $\underline{p}^{(1)}$ to $\underline{p}^{(2)}$, by the angle required to align the image of that line-segment with the $z$-axis is then carried out. We allow $\underline{\lambda}^{(i)}$ to denote the shifted and rotated line segment obtained by transforming $\underline{L}^{(i)}$ in this way, with end points $\underline{\lambda}^{(i)}(0)$ and $\underline{\lambda}^{(i)}(1)$.

Under our model, we expect observed MT trajectories to initiate at (0, 0, ±$b$) and to terminate at the plane $z$=0. We orient each trajectory so that it is consistent with this. This allows us to specify that $\underline{\lambda}^{(i)}(0)$ is the end of each line segment closest to a fixed point and $\underline{\lambda}^{(i)}(1)$ the end closest to the plane that models the metaphase plate.

Journal of Cell Science (2017) 130, 1845-1855 doi:10.1242/jcs.203877

Our interest is focused on those MTs leading from the spindle pole to the metaphase plate and so our analysis is restricted to observed lines for which the $z$-coordinate lies always in $[-b,+b]$.

## Model directions

We wish to compare the direction of observed lines $\underline{\lambda}^{(i)}$, conveniently denoted $\underline{\delta}^{(i)} = \underline{\lambda}^{(i)}(1) - \underline{\lambda}^{(i)}(0)$, with those consistent with the spheroid model. The first step is to determine the tangent to the geodesic path that passes through the fixed points (0,0, $b$), (0,0, $-b$) and the midpoint of the observed line $\underline{\lambda}^{(i)}$, given by $\underline{\mu}^{(i)} = (\underline{\lambda}^{(i)}(0) + \underline{\lambda}^{(i)}(1))/2$, on the surface of the spheroid.

The unique spheroid which passes through $\underline{\mu}^{(i)}$ and both (0,0, $b$) and (0,0, $-b$) is determined by the value of $a^{(i)}$ given by:

$$\frac{(\mu_x^{(i)})^2 + (\mu_y^{(i)})^2}{(a^{(i)})^2} + \frac{(\mu_z^{(i)})^2}{b^2} = 1 \Rightarrow (a^{(i)})^2 = b^2 \frac{(\mu_x^{(i)})^2 + (\mu_y^{(i)})^2}{b^2 - (\mu_z^{(i)})^2}. \quad (2)$$

The unique tangent to the path at that point is ascertained by standard geometric arguments and is given by:

$$\underline{\rho}(\underline{\mu}^{(i)}) = \left(\mu_x^{(i)}, \mu_y^{(i)}, \frac{(\mu_z^{(i)})^2 - b^2}{\mu_z^{(i)}}\right). \quad (3)$$

This tangent, at a point corresponding to the midpoint of the MT segment, is most likely to align with the original MT set. Comparison could be made between $\underline{\rho}(\underline{\mu}^{(i)})$ and $\underline{\delta}^{(i)}$. However, the earlier remark that all observed lines $\underline{L}^{(i)}$ lie within parallel planes means that even if the MT trajectories exactly follow the ellipsoid model proposed, $\underline{\delta}^{(i)}$ and $\underline{\rho}(\underline{\mu}^{(i)})$ will not be identical. This discrepancy may be removed by comparing $\underline{\delta}^{(i)}$ to $\tilde{\underline{\rho}}(\underline{\mu}^{(i)})$, the projection of $\underline{\rho}(\underline{\mu}^{(i)})$ into the observation planes.

In the original orientation, lines $\underline{L}^{(i)}(t)$ lie in one of the image planes that is perpendicular to the $z$-axis and therefore perpendicular to the vector $\hat{\underline{z}} = (0,0,1)$. After translation and rotation the lines $\underline{\lambda}^{(i)}$ no longer lie in planes perpendicular to $\hat{\underline{z}}$, rather they lie in planes perpendicular to $R\hat{\underline{z}}$ where $R$ is the matrix that characterizes the rotation component of the transformation applied to the original line (in the canonical Euclidean basis). As a result, the projection of proposed directions $\underline{\rho}(\underline{\mu}^{(i)})$ into these planes, $\tilde{\underline{\rho}}(\underline{\mu}^{(i)})$, is given by

$$\tilde{\underline{\rho}}(\underline{\mu}^{(i)}) = \underline{\rho}(\underline{\mu}^{(i)}) - (\underline{\rho}(\underline{\mu}^{(i)}) \cdot R\hat{\underline{z}})R\hat{\underline{z}}. \quad (4)$$

## Model discrepancy and comparison

Angles, denoted by $\theta^{(i)}$, between observed directions, $\underline{\delta}^{(i)}$, and model directions, $\tilde{\underline{\rho}}(\underline{\mu}^{(i)})$, can be calculated as a measure of the discrepancy between observations and the proposed model:

$$\theta^{(i)} = \cos^{-1}\left(\frac{\underline{\delta}^{(i)} \cdot \tilde{\underline{\rho}}(\underline{\mu}^{(i)})}{|\underline{\delta}^{(i)}||\tilde{\underline{\rho}}(\underline{\mu}^{(i)})|}\right). \quad (5)$$

The set of deviations $\Theta = \{\theta^{(1)}, \theta^{(2)}, \ldots, \theta^{(n)}\}$ can be visualized using a histogram as shown in Fig. 5. Note, that systematic variation in the reported angle deviations based on location in the spindle or due to segment length was looked for and no evidence was found.

Analyzing two sets of observations produces two sets of angles, $\Theta_1$ and $\Theta_2$, which may be compared to suggest whether one observation deviates more from the proposed ellipsoid model than the other. We allow $\Pi(\Theta_1, \Theta_2)$ to denote the proportion of all pairs $(\theta, \vartheta) \in \Theta_1 \times \Theta_2$ in which $\theta < \vartheta$:

$$\Pi(\Theta_1, \Theta_2) = \frac{1}{|\Theta_1||\Theta_2|} \sum_{\theta \in \Theta_1,\, \vartheta \in \Theta_2} \mathbf{I}\{\theta < \vartheta\}, \quad (6)$$

where $\mathbf{I}$ denotes the indicator function that takes the value 1 if its argument is true and 0 otherwise. The summary $\Pi(\Theta_1, \Theta_2)$ takes values in [0,1]. Values of $\Pi(\Theta_1, \Theta_2)$ close to 0.5 suggest that the model fits each collection of observations equally well, values below 0.5 suggest that deviations from the model are generally greater for the first set of observations, while values greater than 0.5 suggest that deviations from the model are generally greater for the second set of observations. Comparison using $\Pi$ is preferred to comparison of means as it has greater robustness. Briefly, $\Pi$ has a probabilistic interpretation and compares every element of $\Theta_1$ to every element of $\Theta_2$ rather than comparing a summary statistic of $\Theta_1$ to the corresponding summary statistic of $\Theta_2$. It is less susceptible to measurement error. Addition of random error $\pm\varepsilon$ to each dataset would result in changes to the mean of up to $\pm\varepsilon$, but a only a change in $\Pi$ of $\pm 1/|\Theta_1||\Theta_2|$ for each angle pairing $\theta, \vartheta$. Finally, $\Pi$ is less susceptible to perturbation by outliers.

### Acknowledgements

We thank Heiko Wurdak (Leeds Institute of Cancer and Pathology, University of Leeds, UK) for the gift of glioblastoma cell lines.

### Competing interests

The authors declare no competing or financial interests.

### Author contributions

Conceptualization: A.M.J., J.A.B., S.J.R.; Methodology: F.M.N., A.J.B.; Software: T.R.H., S.J.R.; Validation: T.R.H.; Formal analysis: F.M.N., T.R.H., N.I.C., G.P.S., S.J.R.; Investigation: F.M.N., T.R.H., N.I.C., G.P.S., A.J.B.; Resources: S.J.R.; Writing - original draft: T.R.H., S.J.R.; Writing - review & editing: F.M.N., T.R.H., N.I.C., G.P.S., A.M.J., J.A.B., I.A.P., S.J.R.; Visualization: F.M.N., T.R.H., N.I.C., S.J.R.; Supervision: A.M.J., J.A.B., I.A.P., S.J.R.; Project administration: S.J.R.; Funding acquisition: S.J.R.

### Funding

This work was supported by a North West Cancer Research Fund Project grant (CR928) and a Senior Cancer Research UK Fellowship (C25425/A15182) to S.J.R.

### Data availability

The modeling code used in this paper can be found at https://github.com/quantixed/VolumeFinder, where a detailed walk-through document is also provided.

### Supplementary information

Supplementary information available online at
http://jcs.biologists.org/lookup/doi/10.1242/jcs.203877.supplemental

### References

**Booth, D. G., Hood, F. E., Prior, I. A. and Royle, S. J.** (2011). A tacc3/ch-tog/clathrin complex stabilises kinetochore fibres by inter-microtubule bridging. *EMBO J.* **30**, 906-919.

**Booth, D. G., Cheeseman, L. P., Prior, I. A. and Royle, S. J.** (2013). Studying kinetochore-fiber ultra-structure using correlative light-electron microscopy. *Methods Cell Biol.* **115**, 327-342.

**Chozinski, T. J., Halpern, A. R., Okawa, H., Kim, H.-J., Tremel, G. J., Wong, R. O. L. and Vaughan, J. C.** (2016). Expansion microscopy with conventional antibodies and uorescent proteins. *Nat. Methods* **13**, 485-488.

**Cimini, D., Howell, B., Maddox, P., Khodjakov, A., Degrassi, F. and Salmon, E. D.** (2001). Merotelic kinetochore orientation is a major mechanism of aneuploidy in mitotic mammalian tissue cells. *J. Cell Biol.* **153**, 517-527.

**Elting, M. W., Hueschen, C. L., Udy, D. B. and Dumont, S.** (2014). Force on spindle microtubule minus ends moves chromosomes. *J. Cell Biol.* **206**, 245-256.

**Gergely, F., Karlsson, C., Still, I., Cowell, J., Kilmartin, J. and Raff, J. W.** (2000). The tacc domain identifies a family of centrosomal proteins that can interact with microtubules. *Proc. Natl. Acad. Sci. USA* **97**, 14352-14357.

**Gergely, F., Draviam, V. M. and Raff, J. W.** (2003). The ch-tog/xmap215 protein is essential for spindle pole organization in human somatic cells. *Genes Dev.* **17**, 336-341.

**Gutiérrez-Caballero, C., Burgess, S. G., Bayliss, R. and Royle, S. J.** (2015). Tacc3-ch-tog track the growing tips of microtubules independently of clathrin and aurora-a phosphorylation. *Biol. Open* **4**, 170-179.

**Helmke, K. J., Heald, R. and Wilbur, J. D.** (2013). Interplay between spindle architecture and function. *Int. Rev. Cell Mol. Biol.* **306**, 83-125.

**Hepler, P. K., McIntosh, J. R. and Cleland, S.** (1970). Intermicrotubule bridges in mitotic spindle apparatus. *J. Cell Biol.* **45**, 438-444.

**Hood, F. E., Williams, S. J., Burgess, S. G., Richards, M. W., Roth, D., Straube, A., Pfuhl, M., Bayliss, R. and Royle, S. J.** (2013). Coordination of adjacent domains mediates tacc3-ch-tog-clathrin assembly and mitotic spindle binding. *J. Cell Biol.* **202**, 463-478.

**Hughes, L., Hawes, C., Monteith, S. and Vaughan, S.** (2014). Serial block face scanning electron microscopy–the future of cell ultrastructure imaging. *Protoplasma* **251**, 395-401.

**Kajtez, J., Solomatina, A., Novak, M., Polak, B., Vukušić, K., Rüdiger, J., Cojoc, G., Milas, A., Šumanovac Šestak, I., Risteski, P. et al.** (2016). Overlap microtubules link sister k-fibres and balance the forces on bi-oriented kinetochores. *Nat. Commun.* **7**, 10298.

**Lin, C.-H., Hu, C.-K. and Shih, H.-M.** (2010). Clathrin heavy chain mediates tacc3 targeting to mitotic spindles to ensure spindle stability. *J. Cell Biol.* **189**, 1097-1105.
**Mastronarde, D. N., McDonald, K. L., Ding, R. and McIntosh, J. R.** (1993). Interpolar spindle microtubules in ptk cells. *J. Cell Biol.* **123**, 1475-1489.
**McDonald, K. L., O'Toole, E. T., Mastronarde, D. N. and McIntosh, J. R.** (1992). Kinetochore microtubules in ptk cells. *J. Cell Biol.* **118**, 369-383.
**McEwen, B. F., Heagle, A. B., Cassels, G. O., Buttle, K. F. and Rieder, C. L.** (1997). Kinetochore fiber maturation in ptk1 cells and its implications for the mechanisms of chromosome congression and anaphase onset. *J. Cell Biol.* **137**, 1567-1580.
**McEwen, B. F., Ding, Y. and Heagle, A. B.** (1998). Relevance of kinetochore size and microtubule-binding capacity for stable chromosome attachment during mitosis in ptk1 cells. *Chromosome Res.* **6**, 123-132.
**McIntosh, J. R., O'Toole, E., Zhudenkov, K., Morphew, M., Schwartz, C., Ataullakhanov, F. I. and Grishchuk, E. L.** (2013). Conserved and divergent features of kinetochores and spindle microtubule ends from five species. *J. Cell Biol.* **200**, 459-474.
**Mikhaylova, M., Cloin, B. M. C., Finan, K., van den Berg, R., Teeuw, J., Kijanka, M. M., Sokolowski, M., Katrukha, E. A., Maidorn, M., Opazo, F. et al.** (2015). Resolving bundled microtubules using anti-tubulin nanobodies. *Nat. Commun.* **6**, 7933.
**Nixon, F. M., Gutiérrez-Caballero, C., Hood, F. E., Booth, D. G., Prior, I. A. and Royle, S. J.** (2015). The mesh is a network of microtubule connectors that stabilizes individual kinetochore fibers of the mitotic spindle. *Elife* **4**, e07635.
**Petry, S.** (2016). Mechanisms of mitotic spindle assembly. *Annu. Rev. Biochem.* **85**, 659-683.
**Puhka, M., Vihinen, H., Joensuu, M. and Jokitalo, E.** (2007). Endoplasmic reticulum remains continuous and undergoes sheet-to-tubule transformation during cell division in mammalian cells. *J. Cell Biol.* **179**, 895-909.
**Puhka, M., Joensuu, M., Vihinen, H., Belevich, I. and Jokitalo, E.** (2012). Progressive sheet-to-tubule transformation is a general mechanism for endoplasmic reticulum partitioning in dividing mammalian cells. *Mol. Biol. Cell* **23**, 2424-2432.
**Redemann, S., Baumgart, J., Lindow, N., Fuerthauer, S., Nazockdast, E., Kratz, A., Prohaska, S., Brugues, J., Shelley, M., and Mueller-Reichert, T.** (2016). Kinetochore microtubules indirectly link chromosomes and centrosomes in *C. elegans* mitosis. *bioRxiv*.
**Rieder, C. L.** (1981). The structure of the cold-stable kinetochore fiber in metaphase ptk1 cells. *Chromosoma* **84**, 145-158.
**Schweizer, N., Pawar, N., Weiss, M. and Maiato, H.** (2015). An organelle-exclusion envelope assists mitosis and underlies distinct molecular crowding in the spindle region. *J. Cell Biol.* **210**, 695-704.
**Sikirzhytski, V., Magidson, V., Steinman, J. B., He, J., Le Berre, M., Tikhonenko, I., Ault, J. G., McEwen, B. F., Chen, J. K., Sui, H. et al.** (2014). Direct kinetochore-spindle pole connections are not required for chromosome segregation. *J. Cell Biol.* **206**, 231-243.
**Tolić, I. M. and Pavin, N.** (2016). Bridging the gap between sister kinetochores. *Cell Cycle* **15**, 1169-1170.
**Weber, B., Greenan, G., Prohaska, S., Baum, D., Hege, H.-C., Muller-Reichert, T., Hyman, A. A. and Verbavatz, J.-M.** (2012). Automated tracing of microtubules in electron tomograms of plastic embedded samples of caenorhabditis elegans embryos. *J. Struct. Biol.* **178**, 129-138.